Current-driven collective dynamics of non-Hermitian edge vibrations in armchair graphene nanoribbons

Wen-Hao Mao ⬤, Man-Yu Shang ⬤, and Jing-Tao Lü ⬤*

*School of Physics, Institute for Quantum Science and Engineering and Wuhan National High Magnetic Field Center,
Huazhong University of Science and Technology, Wuhan 430074, People's Republic of China*

We study non-Hermitian collective dynamics of spatially separated edge carbon dimer vibrations in armchair graphene nanoribbons, mediated by coherent and dissipative coupling to nonequilibrium electron transport. We show that the indirect coupling between two dimers depends crucially on gating and source-drain bias. In particular, we analyze the competition between two distinctly different energy transfer mechanism from nonequilibrium electrons to vibrations. One is the deterministic work done by nonconservative current-induced force, and the other is stochastic Joule heating. We find that the effect of the former can be effectively tuned electrically through gating and bias. Our work suggests that armchair graphene nanoribbons could serve as promising candidates in the experimental search for signatures of nonconservative current-induced forces in nanoconductors, which remains elusive despite intense theoretical study.

I. INTRODUCTION

Electron-phonon interaction (EPI) is ubiquitous in solid state and molecular systems and is responsible for many intriguing physics, from Cooper pair formation in superconductivity to Joule heating in various devices. Quantitative understanding of EPI is thus of vital importance from both fundamental and application points of view. Theoretical modeling of EPI normally treats different phonon modes independently within the harmonic approximation, e.g., in the calculation of electron-phonon scattering processes [1].

In fact, even in the harmonic approximation, simultaneous coupling to the electronic system may generate indirect coupling among different, especially degenerate, phonon modes. On the one hand, taking into account this indirect coupling mediated by electrons, it has been shown that under nonequilibrium conditions with electrical current, deterministic work can be done from electrons to phonons through nonconservative current-induced forces (CIFs) [2]. Moreover, an effective magnetic field emerges, which originates from the Berry phase of nonequilibrium electrons [3]. The nonconservative CIFs offer a novel energy transfer mechanism through deterministic work from electron to phonon subsystem, distinctly different from stochastic Joule heating. Several interesting predictions have been put forward in the literature. Dundas *et al*. illustrated using a tight-binding model the ability of nonconservative CIFs to perform work and drive an atomic waterwheel or motor [2]. Bustos-Marún *et al*. analyzed the efficiency of current-driven motors [4]. One of the authors has studied the interplay of stochastic Joule heating and deterministic work performed by nonconservative forces [5]. Despite these theoretical predictions, experimental

observation of nonconservative nature of CIFs remains elusive. Only indirect evidence was inferred in the breaking of Au and Pt atomic chains [6,7]. Thus, it is desirable to explore more systems where the nonconservative CIFs may play dominant roles. In order for the nonconservative force to perform work, there should be at least two vibrational modes such that an enclosed loop in mode space can be formed. Moreover, in order for the CIFs to play dominant roles, the two modes should be nearly degenerate and isolated from the phonon environment.

On the other hand, EPI offers an interesting mechanism to couple otherwise spectrally independent or spatially separated phonon modes through nonequilibrium electrons which serve as a "bus". This results in an effective non-Hermitian phonon system which is tunable electrically. It has been shown that in the presence of time reversal or space inversion symmetry breaking, phonons may acquire nonzero angular momentum due to electron-mediated coupling [3,8–13]. Similar mechanism has proved useful in hybrid quantum devices, including electron or phonon mediated magnon coupling in spin Seebeck effect [14], cavity-mediated vibrational coupling in optomechanical systems [15], spin dynamics [16], etc.

In this work, we choose graphene nanoribbons (GNRs) to further explore these aspects of EPI. Nanostructured graphene has received considerable attention in the past due to its potential electronic and optoelectronic applications in future nanoscale devices [17]. Recent experimental progress has made it possible to fabricate atomically precise nanoribbon structures from a chemical bottom-up approach [18,19]. The ability to tune electron chemical potential through gating in GNRs offers great opportunities to explore electron-mediated vibrational dynamics under nonequilibrium situations. Unlike graphene, GNRs have energy gaps which can be tuned by many means, such as changing ribbon width and edge properties like passivation [20–25], or by apply-

---

*jtlu@hust.edu.cn

085419-1

ing transverse electric field [26,27]. This gap, absent in graphene, results from quantum confinement in the width direction. Previous research has shown that GNRs host specific vibration modes in addition to those modes in pristine graphene [28–35].

We study current-driven non-Hermitian vibrational dynamics of carbon dimers at the boundaries of armchair GNRs. The nearly degenerate, spatially separated dimer vibrations are coupled through electrical current. Their non-Hermitian dynamics can be tuned by changing the average Fermi level (E_F) and the applied voltage bias (V). We find regions of the two-dimensional parameter space (E_F, V) where the nonconservative CIFs are dominant, which results in drastic increase of the total energy in the dimer vibrations. The tunability of GNRs makes them better candidates for experimental search of signatures of nonconservative CIFs, which have remained elusive despite past intense theoretical study [2,3,36–41].

II. THEORY

A. General theory

Our theory has been described in detail in previous works [37,42]. Here, for completeness, we give an outline of the main idea. We start from the standard two-probe transport setup where we divide the whole system into left and right electrodes and the central device. In each part, there are electron and phonon degrees of freedom. We only include EPI in the central device region. We are interested in the vibrational dynamics in the central region. We follow the open system approach and integrate out the nonequilibrium electron subsystem (including both electrodes and central device parts) and phonons in the electrodes. This procedure results in a semiclassical generalized Langevin equation describing the central vibrational modes, hereafter denoted as system

$$\ddot{\mathbf{u}} = -\mathbf{K} \cdot \mathbf{u} - \int dt' \mathbf{\Pi}^r(t - t') \cdot \mathbf{u}(t') + \mathbf{f}(t). \qquad (1)$$

Here, $\mathbf{u}$ is the displacement vector of the system, $\mathbf{K}$ is the dynamical matrix in the harmonic approximation. We have ignored anharmonic effect in this work. The last two terms on the right-hand side are contributions from the environment, representing the deterministic and the fluctuating forces, respectively. The corresponding effective dynamical matrix $\tilde{\mathbf{K}}$ after including the influence of the environment is written in the frequency domain as

$$\widetilde{\mathbf{K}}[\omega] = \mathbf{K} + \mathbf{\Pi}^r[\omega], \qquad (2)$$

where $\mathbf{\Pi}^r[\omega]$ is the retarded self-energy in the nonequilibrium Green's function theory due to coupling to the environment. Here, we concentrate on the coupling to nonequilibrium electronic environment and ignore the coupling to phononic environment. This is applicable to the dimer vibrations in armchair GNRs. The fluctuating force $\mathbf{f}$ is characterized by the correlation function, which only depends on the time difference. This allows us to make the Fourier transform and

write it in the frequency domain

$$\hat{\Pi}_{kl}[\omega] = \int dt \langle f_k(t) f_l(0) \rangle e^{i\omega t}$$

$$= -\pi \Lambda_{kl}(\omega) \coth\left(\frac{\hbar\omega}{2k_B T}\right) - \pi \sum_{\alpha\beta} \Lambda_{kl}^{\alpha\beta}(\omega)$$

$$\times \left[\coth\left(\frac{\hbar\omega - (\mu_\alpha - \mu_\beta)}{2k_B T}\right) - \coth\left(\frac{\hbar\omega}{2k_B T}\right) \right], \qquad (3)$$

with the electron-vibration coupling weighted electron-hole pair density of states

$$\Lambda_{kl}^{\alpha\beta}(\omega) = 2 \int \frac{d\varepsilon_1}{2\pi} \int \frac{d\varepsilon_2}{2\pi} \delta(\hbar\omega - \varepsilon_1 + \varepsilon_2)$$

$$\times \mathrm{Tr}[\mathbf{M}^k \mathbf{A}_\alpha(\varepsilon_1) \mathbf{M}^l \mathbf{A}_\beta(\varepsilon_2)]$$

$$\times [n_F(\varepsilon_1 - \mu_\alpha) - n_F(\varepsilon_2 - \mu_\beta)]. \qquad (4)$$

Here, $\mathbf{M}^{k/l}$ is the electron-vibration coupling matrix for mode k/l, $\mathbf{A}_\alpha$ is the electron spectral function contributed by scattering states from electrode α, $n_F(\varepsilon) = [\exp(\varepsilon/k_B T) + 1]^{-1}$ is the Fermi-Dirac distribution, and μ_α, T are the chemical potential and temperature, respectively.

Excitation of the vibrational modes can be studied by solving the generalized Langevin equation in the frequency domain. The displacement correlation function is written as

$$\langle \mathbf{u}\mathbf{u}^T \rangle(\omega) = \mathbf{D}^r(\omega) \hat{\mathbf{\Pi}}(\omega) \mathbf{D}^a(\omega), \qquad (5)$$

where the retarded vibration Green's function is

$$\mathbf{D}^r(\omega) = \frac{1}{(\omega + i\delta)^2 \mathbf{I} - \tilde{\mathbf{K}}(\omega)}, \qquad (6)$$

and

$$\mathbf{D}^a = (\mathbf{D}^r)^\dagger. \qquad (7)$$

The energy stored in the vibrational system can then be obtained from

$$E = \int \frac{d\omega}{2\pi} \omega^2 \mathrm{Tr}[\langle \mathbf{u}\mathbf{u}^T \rangle(\omega)]. \qquad (8)$$

This setup has been used to study current-driven vibrational dynamics in atomic and molecular junctions [42], nanoelectromechanical systems [36,43], and molecular dynamics on metal surfaces [39]. It has been found that the real and imaginary parts of $\mathbf{\Pi}^r$ can be divided into *symmetric* and *antisymmetric* parts, respectively. The symmetric real part describes renormalization of the dynamical matrix, and the antisymmetric real part corresponds to the nonconservative CIF. The symmetric imaginary part is the electronic friction, and the corresponding antisymmetric part behaves as an effective Lorentz force due to Berry phase of nonequilibrium electrons [3,38,43,44]. While both the renormalization and electronic friction are present in equilibrium, the nonconservative CIF and effective Lorentz force are nonzero only in the presence of electrical current. Notably, the nonconservative CIF and the electronic friction render the system non-Hermitian. Finally, we also note that such eigen spectrum analysis used here serves to find possible candidate systems where the CIFs play an important role. To perform further

quantitative analysis, we need to properly take into account the anharmonic vibrational coupling [45] and possible back action of the vibrations on electronic transport. These calculations for realistic systems are highly demanding and are postponed for future work.

B. Eigen mode analysis

We can study the dynamics and heating of the new eigen modes after including indirect coupling between carbon dimers through electrical current. We split $\hat{\mathbf{\Pi}}(\omega)$ into two terms

$$\hat{\mathbf{\Pi}}(\omega) = \hat{\mathbf{\Pi}}_0(\omega) + \mathbf{\Delta}\hat{\mathbf{\Pi}}(\omega) \tag{9}$$

with $\hat{\mathbf{\Pi}}_0(\omega)$ representing the equilibrium part and $\Delta\hat{\mathbf{\Pi}}(\omega)$ the Joule heating part

$$\Delta\hat{\mathbf{\Pi}}(\omega) = -\pi \sum_{\alpha\beta} \mathbf{\Lambda}^{\alpha\beta}(\omega)$$
$$\times \left[\coth\left(\frac{\hbar\omega - (\mu_\alpha - \mu_\beta)}{2k_BT}\right) - \coth\left(\frac{\hbar\omega}{2k_BT}\right)\right]. \tag{10}$$

When the broadening of eigen mode i is small, the mode energy can be written as

$$E_i = \frac{\hbar\omega_i}{2}\coth\left(\frac{\hbar\omega_i}{2k_BT}\right) + \frac{\hbar\Delta\hat{\Pi}_{ii}(\omega_i)}{2\eta_i}$$
$$\equiv \left(N_i + \frac{1}{2}\right)\hbar\omega_i. \tag{11}$$

We get an effective phonon occupation number

$$N_i = n_B(\omega_i, T) + \frac{\Delta\hat{\Pi}_{ii}(\omega_i)}{2\omega_i\eta_i}, \tag{12}$$

where $\eta_i = -2\,\text{Im}[\Omega_i]$, $\omega_i = \text{Re}[\Omega_i]$ with Ω_i the complex eigen value of mode i, and $n_B(\omega, T) = [\exp(\hbar\omega/k_BT) - 1]^{-1}$ is the Bose-Einstein distribution.

Now we focus on the calculation of $\Delta\hat{\Pi}_{ii}(\omega_i)$. In order to elucidate the detail, we derive the displacement correlation function in the eigen basis. Because $\widetilde{\mathbf{K}}$ is not Hermitian, it has two spectral decompositions

$$\widetilde{\mathbf{K}}|\mathbf{w}_i\rangle = \lambda_i|\mathbf{w}_i\rangle, \tag{13}$$

$$\langle\mathbf{v}_i|\widetilde{\mathbf{K}} = \lambda_i\langle\mathbf{v}_i| \iff \widetilde{\mathbf{K}}^\dagger|\mathbf{v}_i\rangle = \lambda_i^*|\mathbf{v}_i\rangle, \tag{14}$$

where $\lambda_i = \Omega_i^2$ is ith eigen value of $\widetilde{\mathbf{K}}$, and $|\mathbf{v}_i\rangle$ and $|\mathbf{w}_i\rangle$ are ith left and right eigen vectors respectively. Note that $|\mathbf{v}_i\rangle$ and $|\mathbf{w}_i\rangle$ correspond to the same eigen value and are biorthogonal:

$$\langle\mathbf{v}_i|\mathbf{w}_j\rangle = \delta_{ij}.$$

The phonon retarded Green's function $\mathbf{D}^r(\omega)$ is written in the eigen basis as

$$\mathbf{D}^r(\omega) = \sum_{ij} |\mathbf{w}_i\rangle\langle\mathbf{v}_i| \frac{1}{\omega^2\mathbf{I} - \widetilde{\mathbf{K}}} |\mathbf{w}_j\rangle\langle\mathbf{v}_j|$$
$$= \sum_i \frac{|\mathbf{w}_i\rangle\langle\mathbf{v}_i|}{\omega^2 - \Omega_i^2}. \tag{15}$$

Similarly, the phonon advanced Green's function $\mathbf{D}^a(\omega)$ is

$$\mathbf{D}^a(\omega) = \sum_i \frac{|\mathbf{v}_i\rangle\langle\mathbf{w}_i|}{\omega^2 - \Omega_i^{*2}}. \tag{16}$$

The displacement correlation function is

$$\langle\mathbf{u}\mathbf{u}^T\rangle(\omega) = \mathbf{D}^r(\omega)\hat{\mathbf{\Pi}}(\omega)\mathbf{D}^a(\omega)$$
$$= \sum_{ij} \frac{|\mathbf{w}_i\rangle\langle\mathbf{v}_i|\hat{\mathbf{\Pi}}(\omega)|\mathbf{v}_j\rangle\langle\mathbf{w}_j|}{(\omega^2 - \Omega_i^2)(\omega^2 - \Omega_j^{*2})}. \tag{17}$$

The ith diagonal element is then

$$\langle\mathbf{v}_i|\mathbf{u}\mathbf{u}^T|\mathbf{v}_i\rangle = \frac{\langle\mathbf{v}_i|\hat{\mathbf{\Pi}}(\omega)|\mathbf{v}_i\rangle}{(\omega^2 - \Omega_i^2)(\omega^2 - \Omega_i^{*2})}. \tag{18}$$

This suggests that we should calculate $\Delta\hat{\Pi}_{ii}(\omega_i)$ by

$$\Delta\hat{\Pi}_{ii}(\omega_i) = \langle\mathbf{v}_i|\Delta\hat{\mathbf{\Pi}}(\omega_i)|\mathbf{v}_i\rangle. \tag{19}$$

Finally, utilizing the real parts of time-dependent eigen vectors, we can construct the eigen orbitals, which typically enclose an elliptical area. Use $\mathbf{r}$ to denote a representative point in such an orbital. Via $\mathbf{r}$ and its time derivative $\mathbf{v} = d\mathbf{r}/dt$, we can define an angular momentum $\mathbf{L}$ as

$$\mathbf{L} = \mathbf{r} \times \mathbf{v} = AB\omega \sin\Delta\Phi\,\hat{\mathbf{k}}. \tag{20}$$

Here A, B and $\Delta\Phi$ are the amplitudes and phase difference of the components of the complex eigen vector. ω is the (real part of the) frequency of this eigen mode. $\hat{\mathbf{k}}$ is the unit vector perpendicular to the plane spanned by this eigen orbital. Note that the angular momentum defined above has the dimension of frequency because we have chosen normalized eigen vector ($A^2 + B^2 = 1$) during the calculation. We find that the magnitude (up to a factor $2/\omega$) and sign of $\mathbf{L}$ determine the shape and the orbital direction of the mode respectively (see the Appendix).

III. RESULTS

A. GNR structures

Band gap of armchair GNRs decays with width oscillatorily in a period of three [46]. We choose a width with a band gap of ≈ 0.13 eV. The boundary carbon dimers are hydrogenated forming sp^2 hybridization (Fig. 1). The status of hydrogenation in experimentally fabricated ribbons is difficult to measure and largely unknown. Previous study has suggested using inelastic electron tunneling spectroscopy (IETS) to identify possible dehydrogenated armchair edge vibrations, whose frequencies spill out of the bulk phonon band due to carbon bond contraction [Fig. 2(a), black circle]. These dimer vibrations do not couple to the rest vibrational modes in the harmonic approximation and have a small vibrational damping. This results in an extra IETS signal at the corresponding bias compared to the perfect hydrogenated structure [47]. The electron transmission spectrum [Fig. 1(c)] is also slightly modified due to the presence of dehydrogenated dimers.

Here, we consider only minimum model systems which have two such dimer vibrations and study in details their collective non-Hermitian dynamics due to simultaneous coupling to electron transport. We have checked its validity by comparing the results obtained including all the vibrational
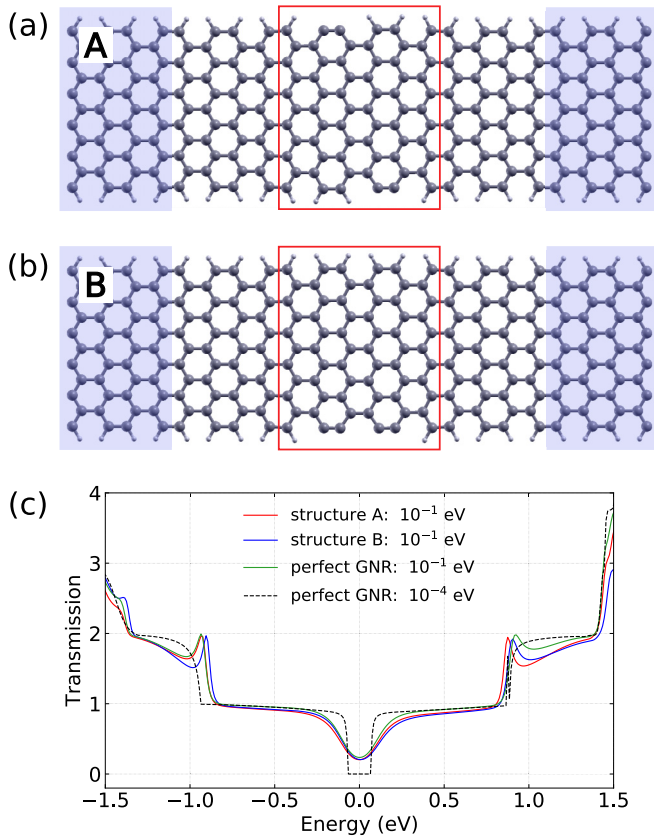
FIG. 1. [(a), (b)] Armchair GNRs with two dehydrogenated carbon dimers at the opposite (A) or same (B) side. The shadow areas on both sides are the electrodes. The vibration modes within red boxes are calculated. (c) Electron transmission spectra of structures A and B and perfect GNR (fully hydrogenated). Different broadenings (10^{-1} and 10^{-4} eV) are added to the electrode self-energy to simulate the coupling to metal electrodes. Larger broadening (10^{-1} eV) smooths out the steplike transmission spectrum and is used in the following calculations.
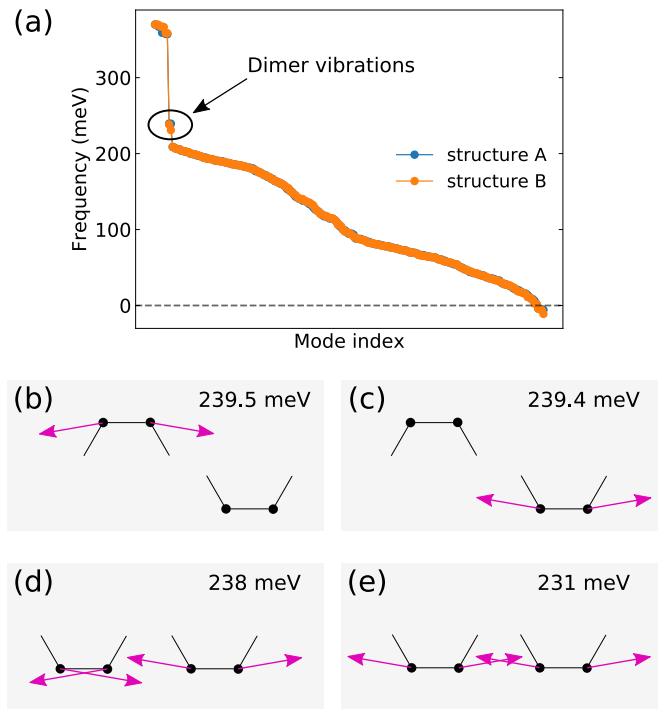

FIG. 2. (a) Vibrational mode spectra of structures A and B for atoms enclosed by red boxes in Figs. 1(a) and 1(b). Modes with frequency >300 meV are C-H vibrations. Those with frequencies at ≈0.24 eV are dimer vibrations at the edges, indicated by the black circle. [(b), (c)] The two dimer vibrations of structure A. The two modes are almost independent of each other. [(d), (e)] The two dimer vibrations of structure B. Both involve motion of the two dimers. Mode in panel (d) is out of phase, while that in panel (e) is in phase. The eigen frequencies shown in panels (b)–(e) are obtained without including their coupling to electrons.

modes in both equilibrium and nonequilibrium situations. The typical structures we investigate in this work are shown in Figs. 1(a) and 1(b). Other types of relative position of the dimers at the edges are also studied, and similar results are found. Structures A and B have two dimers at the opposite and same sides of the ribbon, respectively. The direct atomic coupling between the two dimers in structure B is stronger due to their closer spatial distance, resulting in larger frequency splitting of the two vibrational modes. The corresponding atomic motion is depicted in Figs. 2(b) and 2(c) for structure A and Figs. 2(d) and 2(e) for structure B. The two dimers in A are largely decoupled, while those in B couple together and form a pair of in-phase and out-of-phase vibrational modes.

The calculations are performed using density functional theory calculation combined with nonequilibrium Green's function method as implemented in SIESTA-TranSIESTA [48–51]. We use the PBE version of the generalized gradient approximation [52] for the exchange-correlation functional, single-ζ polarization for the basis sets of carbon and hydrogen atoms with an energy cutoff of 200 Ry for the real space grid. All the structures are relaxed until the

force on each atom in the device region is less than 0.02 eV/Å. This set of parameters has been used in previous works and shows reasonable balance between computation accuracy and cost [47]. The vibrational spectra and the electron-vibration coupling matrix are calculated for atoms in the red boxes in Figs. 1(a) and 1(b) using the Inelastica toolkit [53].

B. Coupled carbon dimer dynamics

We have calculated the total energy $E = \sum_i \hbar \omega_i N_i$, excluding zero-point energy, stored in the two new eigen modes when including CIFs as a function of the equilibrium Fermi level E_F and the voltage bias V, as is shown in Fig. 3. Before discussing the main results, we note that when the voltage bias V is below the vibrational energy ($|eV| < \hbar \omega$), there is no vibrational excitation. All the results in Fig. 3 show this threshold behavior. We also note that since single-molecule Raman spectroscopy can be performed on current-carrying molecular junctions, the effective phonon number deduced from energy can in principle be measured by optical spectroscopy.

By tuning E_F and V, we can locate the parameter space where the nonconservative CIF becomes dominant. This corresponds to bright regions in Fig. 3(a), where the total energy stored in these two modes is orders of magnitude higher than
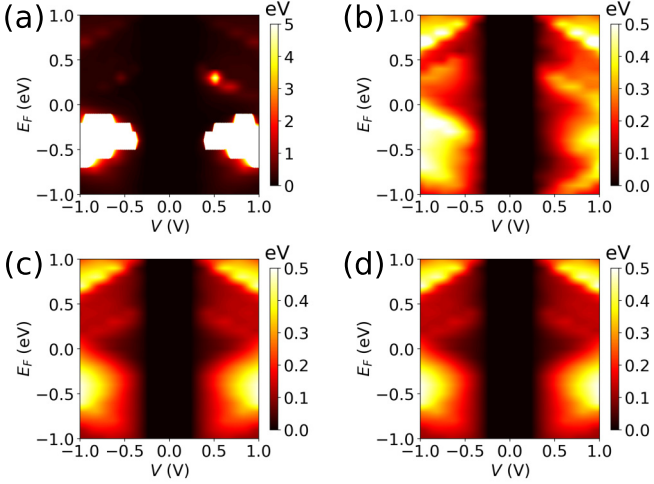
FIG. 3. Contour plot of total energy stored in the two vibrational modes as a function of voltage bias V and average Fermi energy E_F for structures A and B at steady state. [(a), (b)] Structure A with and without nonconservative and effective Lorentz forces. [(c), (d)] Structure B with and without nonconservative and effective Lorentz forces. Note the different color scale between panels (a) and (b)–(d). The effect of nonconservative CIFs is reflected in the order-of-magnitude increase of the total energy at several regions of the parameter space in panel (a).

the rest region. In these cases, the dominant energy transfer mechanism is the deterministic work done by nonconservative CIF, instead of the stochastic Joule heating. For this to happen, there has to be at least two vibrational modes involved. From this point of view, it is a collective behavior, where the energy of the two vibrational modes is much higher than what one single mode would have in the same situation, viz. $1 + 1 \gg 2$. For structure B, no such regions exist, indicating that nonconservative CIF is negligible. The direct atomic coupling of the two dimers in structure B introduces larger frequency splitting and renders the nonconservative CIF less effective, although the CIF in structure B is comparable in magnitude to that in structure A (see Figs. 4 and 5). In the following, we analyze in more details the dynamics of the vibrational modes at representative Fermi level and bias voltage.

1. Voltage bias dependence at fixed E_F

Figures 4 and 5 show the bias dependence of the self-energy $\mathbf{\Pi}^r$ separated into four parts, corresponding to four types of forces, at $E_F = -0.3$ eV for the two structures, respectively. The nonconservative and effective Lorentz force are antisymmetric in the mode indices and only the off-diagonal elements are nonzero. They depend approximately linearly on the bias in the range $[-0.5, 0.5]$ V, consistent with prediction in the wide band limit [42]. Comparing these two structures, we find that the magnitude of these four types of forces are similar for both structures, although the dependence of friction and renormalization on the bias is more complicated.

For structure A, the dependence of various eigen mode characteristics on the bias is shown in Fig. 6. Real parts of the complex eigen frequencies are shown in Fig. 6(a).
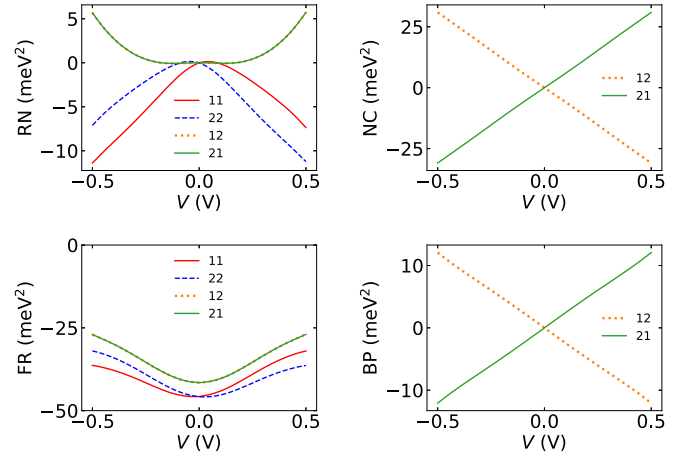

FIG. 4. The four parts of the self-energy $\mathbf{\Pi}^r$ as a function of bias for structure A at $E_F = -0.3$ eV. RN, NC, FR, and BP correspond to the real symmetric, real antisymmetric, imaginary symmetric, and imaginary antisymmetric parts of $\mathbf{\Pi}^r$, representing renormalization of the dynamical matrix, nonconservative CIF, electronic friction, and effective Lorentz force due to Berry phase of electrons, respectively. The mode indices 1 and 2 correspond to the high- and low-frequency modes in Fig. 2, respectively.

The frequency splitting is on the order of 10^{-2} meV. This indicates that the EPI is rather weak. However, since the original frequency splitting without coupling to electrons is also small (≈ 0.1 meV), the CIFs are quite effective to influence the dimer vibrations. The inverse Q factor, defined as $1/Q_i = \eta_i/\omega_i$, is shown in Fig. 6(b). For one eigen mode (red line) $1/Q$ decreases to zero when bias exceeds some threshold value, ≈ 0.5 and -0.45 V at positive and negative polarities. The corresponding effective phonon number N grows sharply when the bias approaches the threshold [Fig. 6(c)]. The connection between $1/Q$ and N is rooted in the friction coefficient η_i, which enters the denominator in Eq. [12]. When $1/Q$ approaches zero, the effective phonon number diverges, indicating a vibrational instability and breakdown of harmonic approximation.

Figure 6(d) shows the dependence of the angular momentum $\mathbf{L}$ of eigen orbitals on the bias. The corresponding eigen
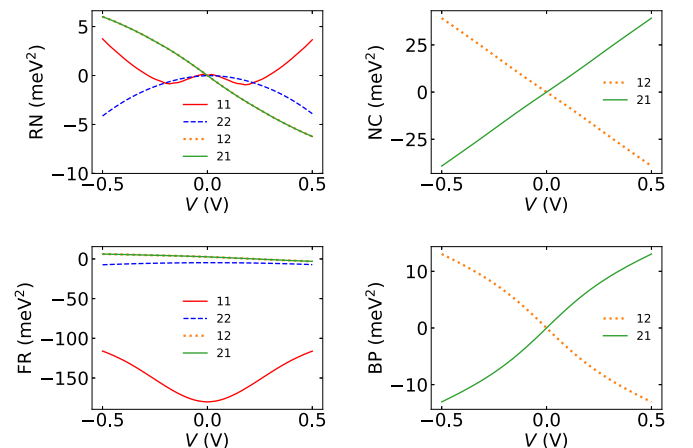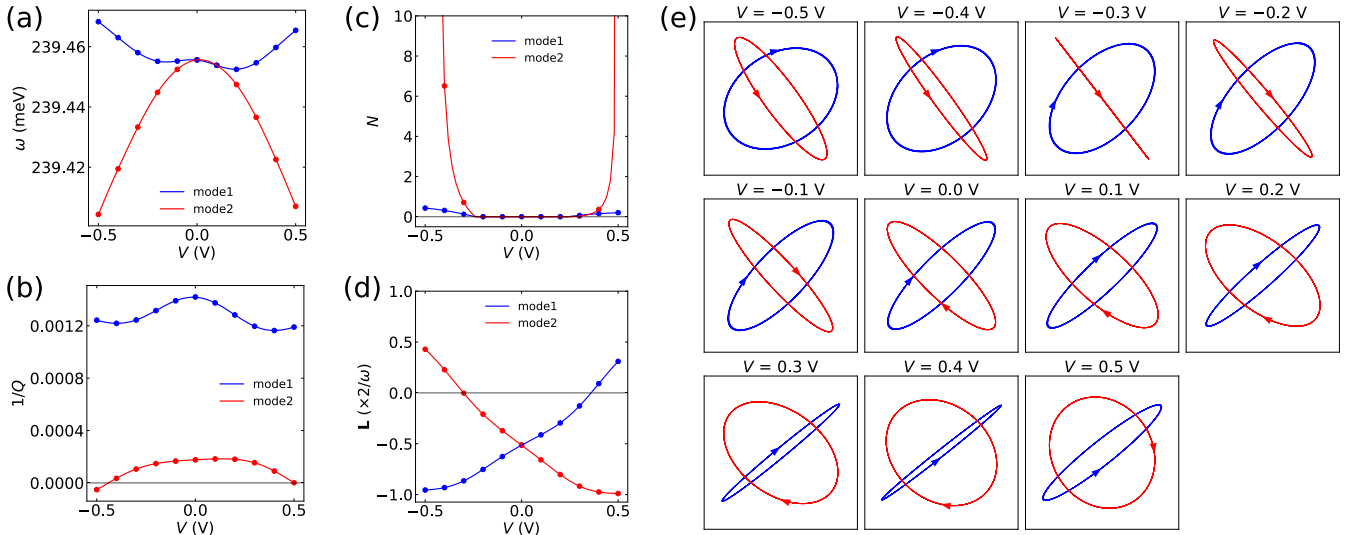

FIG. 5. Similar to Fig. 4 for structure B.

FIG. 6. Bias dependence of real part of eigen frequency (a), inverse Q factor (b), effective phonon number (c), angular momentum (d), and the corresponding eigen orbitals (e) for structure A at $E_F = -0.3$ eV. Note that the angular momentum shown in panel (d) is multiplied by $2/\omega$ to be dimensionless. The resulting quantity $2\mathbf{L}/\omega$ is closely related to the shape of eigen orbitals in panel (e); that is, an absolute "1" corresponds to a circle and "0" to a line (see the Appendix).

orbitals are shown in Fig. 6(e). The sign of $\mathbf{L}$ determines the rotation direction of the eigen orbital and its magnitude determines the shape, which is confirmed by the results in Figs. 6(d) and 6(e). For example, with the bias adjusted from -0.5 to $+0.5$ V, $\mathbf{L}$ of the mode represented by red line changes sign at ≈ -0.3 V and its magnitude first decreases and then increases. Correspondingly, the orbital changes the rotation direction at ≈ -0.3 V and its shape first deforms to a line then recovers to an ellipse. It is worthy noting that both orbitals follow the clockwise direction with negative angular momentum at zero bias. This is due to their dissipative coupling through the off-diagonal electronic friction. As shown, the two modes exhibit opposite bias dependences and each of them changes the orbital direction upon increasing bias in the two polarities.

We have checked that change of $\mathbf{L}$ is mainly determined by the phase difference $\Delta\Phi$ of the two eigen vector components, which is further determined by the bias-dependent nonconservative CIF. The absolute magnitude AB, on the other hand, changes little with bias.

Since the nonconservative force has a nonzero curl in the mode space formed by the two dimers, the orbit that goes in the "correct" direction can gain energy from the nonconservative force field, which results in deterministic work input to this mode. This correct direction turns out to be clockwise in the positive bias polarity and anticlockwise in the negative polarity. This is the physical reason why one of the modes (red) is excited much larger than the other one (blue).

Similar results for structure B are shown in Fig. 7. Due to stronger atomic coupling between the two dimers, effects of the nonconservative CIF are much weaker. The collective effect ceases to play any role. The excitation of the two modes
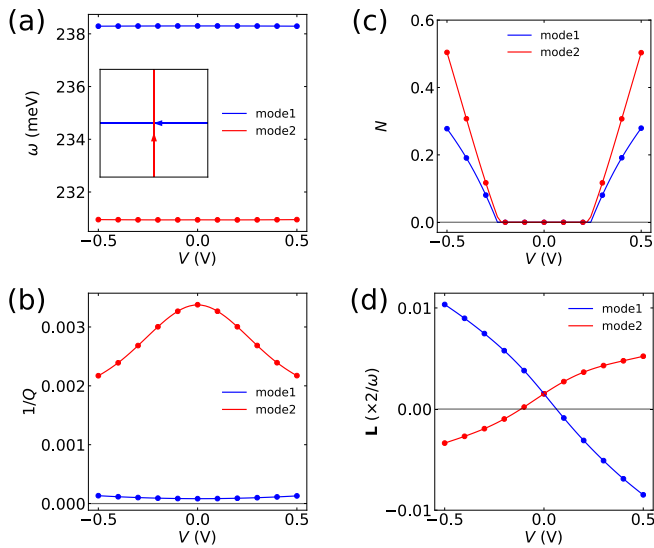

FIG. 7. [(a)–(d)] Similar to Fig. 6 for structure B. Inset of (a): Eigen orbital at zero bias. Note that the scale in panel (d) is different from that in Fig. 6(d).
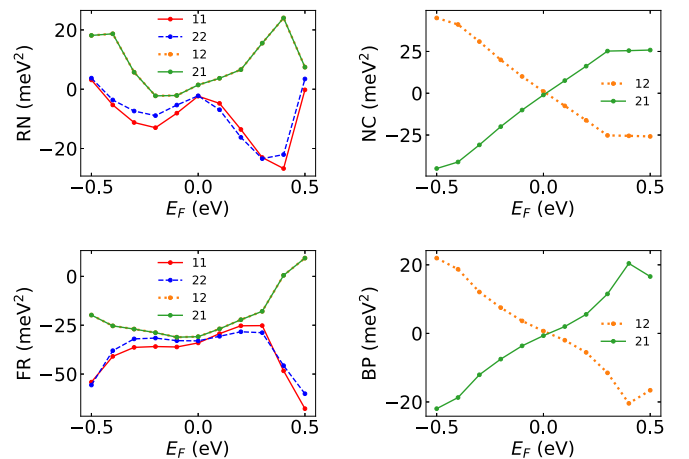

FIG. 8. The four parts of the self-energy $\mathbf{\Pi}^r$ as a function of gating E_F for structure A at bias $V = 0.5$ V.
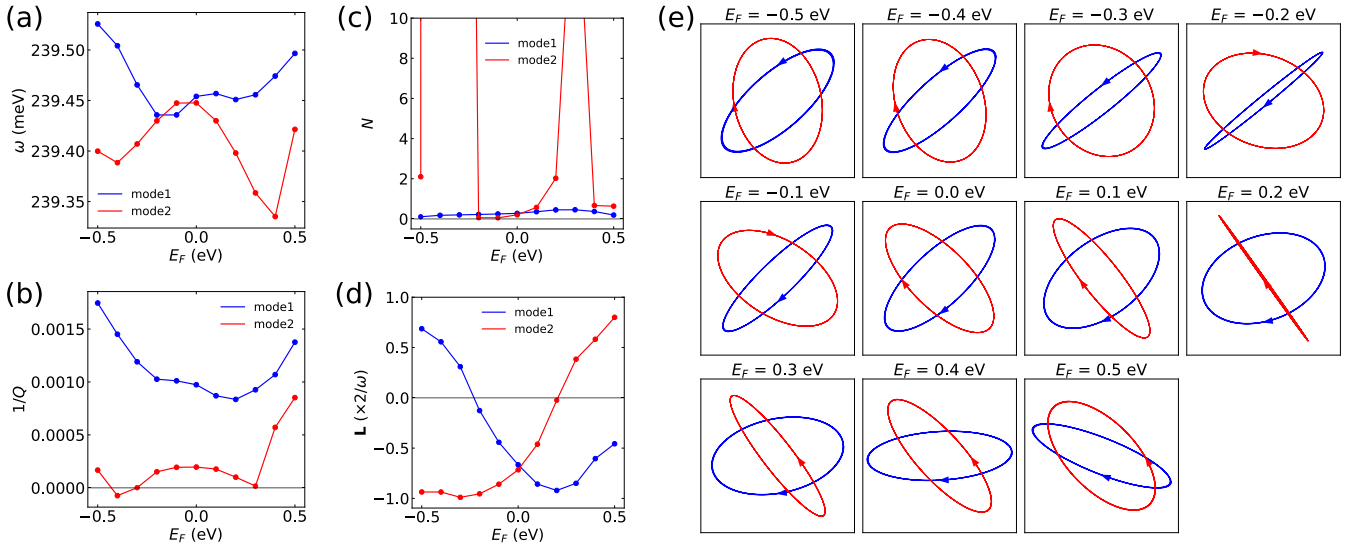
FIG. 9. Dependence of real part of eigen frequency (a), inverse Q factor (b), effective phonon number (c), angular momentum (d), and the corresponding eigen orbitals (e) on E_F for structure A at bias $V = 0.5$ V.

is mainly due to stochastic Joule heating, with the magnitude much smaller than that in structure A. The presence of one mode has little effect on heating of the other mode, and thus $1 + 1 \approx 2$. Both modes have orbital angular momentum close to zero, as is shown in Fig. 7(d). The corresponding eigen orbitals almost collapse to lines [see inset of Fig. 7(a)] and shows little bias dependence (not shown).

2. E_F dependence at fixed voltage bias

Similar analysis can be done by changing E_F at fixed V. For structure A, the results in Fig. 8 show that both the non-conservative and effective Lorentz force vary approximately linearly with E_F and change sign when passing $E_F = 0$, where the majority current carriers change from electrons at $E_F > 0$ to holes at $E_F < 0$. The corresponding angular momentum and orbital shape change with E_F similar to their V dependence, as shown in Fig. 9. While for structure B, the effects of CIFs are again negligible (not shown).

IV. CONCLUSIONS

In summary, we have studied the coupled dynamics of edge vibrations at armchair GNRs mediated by nonequilibrium electron transport. This coupling is tunable electrically in a two-dimensional space of gate and source-drain bias. The dimer vibrations we focused on here are localized in real space and in the vibrational spectrum of the ribbon. This greatly simplifies our analysis, such that we can concentrate on the effect of electron bath. We show that armchair GNRs are better candidates to explore the effects of CIFs on the vibrational dynamics than atomic chains or molecular junctions, where electrostatic gating is difficult to realize.

ACKNOWLEDGMENT

APPENDIX: THE ORBITAL SHAPE, ORIENTATION, AND ANGULAR MOMENTUM

Use $\mathbf{r} = [r_1, r_2]^T$ to represent the gate- and bias-dependent eigen vector, the time-dependent components are

$$r_1(t) = A e^{-i\omega t},$$
$$r_2(t) = B e^{i\Delta\Phi} e^{-i\omega t}. \quad \text{(A1)}$$

Here A, B, and $\Delta\Phi$ are the length and relative phase of the two components. With time evolution, the orbit encloses an elliptical area as shown in the main text.

Choose the normalized eigen vector ($A^2 + B^2 = 1$) and use $r = |\mathbf{r}|$ to represent the distance from a point in the orbit to the center; then

$$r^2 = (\text{Re}[r_1])^2 + (\text{Re}[r_2])^2 = \tfrac{1}{2} + \alpha \sin(2\omega t + \beta). \quad \text{(A2)}$$

The maximum and minimum of r^2 are $\tfrac{1}{2} + \alpha$ and $\tfrac{1}{2} - \alpha$ respectively. Here, we define

$$\alpha = \tfrac{1}{2}(1 - F^2)^{1/2}, \quad \text{(A3)}$$

$$F = 2AB \, |\sin \Delta\Phi|, \quad \text{(A4)}$$

$$\tan \beta = \frac{A^2 + B^2 \cos 2\Delta\Phi}{B^2 \sin 2\Delta\Phi}. \quad \text{(A5)}$$

We see that the larger the parameter F is, the fatter the orbit is. In particular, the orbit becomes circular when $F = 1$ and collapses to a line when $F = 0$. We can show that the angular momentum of the orbital is related to F through $F = 2|\mathbf{L}|/\omega$, with ω the angular frequency of the mode.

The orientation of the orbit is characterized by the angle θ between the longer axis of the orbit and the x axis. We have

$$\tan \theta = \frac{B \cos\left(\Delta\Phi + \frac{\beta}{2} - \frac{\pi}{4}\right)}{A \cos\left(\frac{\beta}{2} - \frac{\pi}{4}\right)}. \quad \text{(A6)}$$

[1] G. D. Mahan, *Many-Particle Physics*, 3rd ed. (Springer, New York, 2000).

[2] D. Dundas, E. J. McEniry, and T. N. Todorov, Current-driven atomic waterwheels, Nat. Nanotechnol. **4**, 99 (2009).

[3] J.-T. Lü, M. Brandbyge, and P. Hedegård, Blowing the fuse: Berry's phase and runaway vibrations in molecular conductors, Nano Lett. **10**, 1657 (2010).

[4] R. Bustos-Marún, G. Refael, and F. von Oppen, Adiabatic Quantum Motors, Phys. Rev. Lett. **111**, 060802 (2013).

[5] J.-T. Lü, R. B. Christensen, J.-S. Wang, P. Hedegård, and M. Brandbyge, Current-Induced Forces and Hot Spots in Biased Nanojunctions, Phys. Rev. Lett. **114**, 096801 (2015).

[6] C. Sabater, C. Untiedt, and J. M. van Ruitenbeek, Evidence for non-conservative current-induced forces in the breaking of Au and Pt atomic chains, Beilstein J. Nanotechnol. **6**, 2338 (2015).

[7] M. Ring, D. Weber, P. Haiber, F. Pauly, P. Nielaba, and E. Scheer, Voltage-induced rearrangements in atomic-size contacts, Nano Lett. **20**, 5773 (2020).

[8] L.-H. Hu, J. Yu, I. Garate, and C.-X. Liu, Phonon Helicity Induced by Electronic Berry Curvature in Dirac Materials, Phys. Rev. Lett. **127**, 125901 (2021).

[9] L. Zhang and Q. Niu, Angular Momentum of Phonons and the Einstein–de Haas effect, Phys. Rev. Lett. **112**, 085503 (2014).

[10] L. Zhang and Q. Niu, Chiral Phonons at High-Symmetry Points in Monolayer Hexagonal Lattices, Phys. Rev. Lett. **115**, 115502 (2015).

[11] H. Zhu, J. Yi, M.-Y. Li, J. Xiao, L. Zhang, C.-W. Yang, R. A. Kaindl, L.-J. Li, Y. Wang, and X. Zhang, Observation of chiral phonons, Science **359**, 579 (2018).

[12] H. Chen, W. Wu, J. Zhu, S. A. Yang, and L. Zhang, Propagating chiral phonons in three-dimensional materials, Nano Lett. **21**, 3060 (2021).

[13] H. Chen, W. Wu, J. Zhu, Z. Yang, W. Gong, W. Gao, S. A. Yang, and L. Zhang, Chiral phonon diode effect in chiral crystals, Nano Lett. **22**, 1688 (2022).

[14] H. Adachi, K.-i. Uchida, E. Saitoh, and S. Maekawa, Theory of the spin Seebeck effect, Rep. Prog. Phys. **76**, 036501 (2013).

[15] J. d. Pino, J. J. Slim, and E. Verhagen, Non-Hermitian chiral phononics through optomechanically induced squeezing, Nature (London) **606**, 82 (2022).

[16] U. Bajpai and B. K. Nikolić, Spintronics Meets Nonadiabatic Molecular Dynamics: Geometric Spin Torque and Damping on Dynamical Classical Magnetic Texture due to an Electronic Open Quantum System, Phys. Rev. Lett. **125**, 187202 (2020).

[17] H. Wang, H. S. Wang, C. Ma, L. Chen, C. Jiang, C. Chen, X. Xie, A.-P. Li, and X. Wang, Graphene nanoribbons for quantum electronics, Nat. Rev. Phys. **3**, 791 (2021).

[18] J. Cai, P. Ruffieux, R. Jaafar, M. Bieri, T. Braun, S. Blankenburg, M. Muoth, A. P. Seitsonen, M. Saleh, X. Feng, K. Müllen, and R. Fasel, Atomically precise bottom-up fabrication of graphene nanoribbons, Nature (London) **466**, 470 (2010).

[19] R. M. Jacobberger and M. S. Arnold, High-performance charge transport in semiconducting armchair graphene nanoribbons grown directly on germanium, ACS Nano **11**, 8924 (2017).

[20] F. Ma, Z. Guo, K. Xu, and P. K. Chu, First-principle study of energy band structure of armchair graphene nanoribbons, Solid State Commun. **152**, 1089 (2012).

[21] Y. H. Lu, R. Q. Wu, L. Shen, M. Yang, Z. D. Sha, Y. Q. Cai, P. M. He, and Y. P. Feng, Effects of edge passivation by hydrogen on electronic structure of armchair graphene nanoribbon and band gap engineering, Appl. Phys. Lett. **94**, 122111 (2009).

[22] H. Zheng, Z. F. Wang, T. Luo, Q. W. Shi, and J. Chen, Analytical study of electronic structure in armchair graphene nanoribbons, Phys. Rev. B **75**, 165414 (2007).

[23] P. Wagner, C. P. Ewels, J.-J. Adjizian, L. Magaud, P. Pochet, S. Roche, A. Lopez-Bezanilla, V. V. Ivanovskaya, A. Yaya, M. Rayson, P. Briddon, and B. Humbert, Band gap engineering via edge-functionalization of graphene nanoribbons, J. Phys. Chem. C **117**, 26790 (2013).

[24] X. H. Zheng, L. F. Huang, X. L. Wang, J. Lan, and Z. Zeng, Band gap engineering in armchair-edged graphene nanoribbons by edge dihydrogenation, Comput. Mater. Sci. **62**, 93 (2012).

[25] N. Rosenkranz, C. Till, C. Thomsen, and J. Maultzsch, *Ab initio* calculations of edge-functionalized armchair graphene nanoribbons: Structural, electronic, and vibrational effects, Phys. Rev. B **84**, 195438 (2011).

[26] H. Raza and E. C. Kan, Armchair graphene nanoribbons: Electronic structure and electric-field modulation, Phys. Rev. B **77**, 245434 (2008).

[27] D. S. Novikov, Transverse Field Effect in Graphene Ribbons, Phys. Rev. Lett. **99**, 056802 (2007).

[28] M. Engelund, J. A. Fürst, A. P. Jauho, and M. Brandbyge, Localized Edge Vibrations and Edge Reconstruction by Joule Heating in Graphene Nanostructures, Phys. Rev. Lett. **104**, 036807 (2010).

[29] M. Vandescuren, P. Hermet, V. Meunier, L. Henrard, and P. Lambin, Theoretical study of the vibrational edge modes in graphene nanoribbons, Phys. Rev. B **78**, 195401 (2008).

[30] R. Gillen, M. Mohr, and J. Maultzsch, Symmetry properties of vibrational modes in graphene nanoribbons, Phys. Rev. B **81**, 205426 (2010).

[31] A. V. Savin and Y. S. Kivshar, Vibrational Tamm states at the edges of graphene nanoribbons, Phys. Rev. B **81**, 165418 (2010).

[32] A. V. Savin and Y. S. Kivshar, Surface solitons at the edges of graphene nanoribbons, EPL **89**, 46001 (2010).

[33] T. Hu, J. Zhou, and J. Dong, Vibrational properties and Raman spectra of different edge graphene nanoribbons, studied by first-principles calculations, Phys. Lett. A **377**, 399 (2013).

[34] J. Overbeck, G. B. Barin, C. Daniels, M. L. Perrin, O. Braun, Q. Sun, R. Darawish, M. D. Luca, X.-Y. Wang, T. Dumslaff, A. Narita, K. Müllen, P. Ruffieux, V. Meunier, R. Fasel, and M. Calame, A universal length-dependent vibrational mode in graphene nanoribbons, ACS Nano **13**, 13083 (2019).

[35] A. V. Savin and Y. S. Kivshar, Localized vibrations of graphene nanoribbons, Low Temp. Phys. **42**, 703 (2016).

[36] N. Bode, S. V. Kusminskiy, R. Egger, and F. von Oppen, Scattering Theory of Current-Induced Forces in Mesoscopic Systems, Phys. Rev. Lett. **107**, 036804 (2011).

[37] J.-T. Lü, B.-Z. Hu, P. Hedegård, and M. Brandbyge, Semi-classical generalized Langevin equation for equilibrium and nonequilibrium molecular dynamics simulation, Prog. Surf. Sci. **94**, 21 (2019).

[38] W. Dou and J. E. Subotnik, Perspective: How to understand electronic friction, J. Chem. Phys. **148**, 230901 (2018).

[39] W. Dou, G. Miao, and J. E. Subotnik, Born-Oppenheimer Dynamics, Electronic Friction, and the Inclusion of Electron-Electron Interactions, Phys. Rev. Lett. **119**, 046001 (2017).

[40] R. J. Preston, V. F. Kershaw, and D. S. Kosov, Current-induced atomic motion, structural instabilities, and negative temperatures on molecule-electrode interfaces in electronic junctions, Phys. Rev. B **101**, 155415 (2020).

[41] V. F. Kershaw and D. S. Kosov, Non-adiabatic effects of nuclear motion in quantum transport of electrons: A self-consistent Keldysh–Langevin study, J. Chem. Phys. **153**, 154101 (2020).

[42] J.-T. Lü, M. Brandbyge, P. Hedegård, T. N. Todorov, and D. Dundas, Current-induced atomic dynamics, instabilities, and Raman signals: Quasiclassical Langevin equation approach, Phys. Rev. B **85**, 245444 (2012).

[43] N. Bode, S. V. Kusminskiy, R. Egger, and F. von Oppen, Current-induced forces in mesoscopic systems: A scattering-matrix approach, Beilstein J. Nanotechnol. **3**, 144 (2012).

[44] X. Bian, T. Qiu, J. Chen, and J. E. Subotnik, On the meaning of Berry force for unrestricted systems treated with mean-field electronic structure, J. Chem. Phys. **156**, 234107 (2022).

[45] J.-T. Lü, S. Leitherer, N. R. Papior, and M. Brandbyge, *Ab initio* current-induced molecular dynamics, Phys. Rev. B **101**, 201406(R) (2020).

[46] Y.-W. Son, M. L. Cohen, and S. G. Louie, Energy Gaps in Graphene Nanoribbons, Phys. Rev. Lett. **97**, 216803 (2006).

[47] R. B. Christensen, T. Frederiksen, and M. Brandbyge, Identification of pristine and defective graphene nanoribbons by phonon signatures in the electron transport characteristics, Phys. Rev. B **91**, 075434 (2015).

[48] J. M. Soler, E. Artacho, J. D. Gale, A. García, J. Junquera, P. Ordejón, and D. Sánchez-Portal, The SIESTA method for *ab initio* order-*N* materials simulation, J. Phys.: Condens. Matter **14**, 2745 (2002).

[49] A. García, N. Papior, A. Akhtar, E. Artacho, V. Blum, E. Bosoni, P. Brandimarte, M. Brandbyge, J. I. Cerdá, F. Corsetti, R. Cuadrado, V. Dikan, J. Ferrer, J. Gale, P. García-Fernández, V. M. García-Suárez, S. García, G. Huhs, S. Illera, R. Korytár, P. Koval, I. Lebedeva, L. Lin, P. López-Tarifa, S. G. Mayo, S. Mohr, P. Ordejón, A. Postnikov, Y. Pouillon, M. Pruneda, R. Robles, D. Sánchez-Portal, J. M. Soler, R. Ullah, V. W.-z. Yu, and J. Junquera, SIESTA: Recent developments and applications, J. Chem. Phys. **152**, 204108 (2020).

[50] M. Brandbyge, J.-L. Mozos, P. Ordejón, J. Taylor, and K. Stokbro, Density-functional method for nonequilibrium electron transport, Phys. Rev. B **65**, 165401 (2002).

[51] N. Papior, N. Lorente, T. Frederiksen, A. García, and M. Brandbyge, Improvements on non-equilibrium and transport Green function techniques: The next-generation TRANSIESTA, Comput. Phys. Commun. **212**, 8 (2017).

[52] J. P. Perdew, K. Burke, and M. Ernzerhof, Generalized Gradient Approximation Made Simple, Phys. Rev. Lett. **77**, 3865 (1996).

[53] T. Frederiksen, M. Paulsson, M. Brandbyge, and A.-P. Jauho, Inelastic transport theory from first principles: Methodology and application to nanoscale devices, Phys. Rev. B **75**, 205413 (2007).